

Dense array of elastic hairs obstructing a fluidic channel

Etienne Jambon-Puillet¹

¹LadHyX, CNRS, Ecole Polytechnique, Institut Polytechnique de Paris, Palaiseau, France

(Dated: January 6, 2025)

Dense arrays of soft hair-like structures protruding from surfaces in contact with fluids are ubiquitous in living systems. Fluid flows can easily deform these soft hairs which in turn impacts the flow properties. At the microscale, flows are often confined which exacerbates this feedback loop since the hair deformation has a strong impact on the flow geometry. Here, I investigate experimentally and theoretically pressure driven flows in laminar channels obstructed by a dense array of elastic hairs. I show that the system displays a nonlinear hydraulic resistance that I model by treating the hair bed as a deformable porous media. The porous media height and thus degree of confinement results from the deflection of individual hairs. The resulting fluid-structure interaction model is leveraged to identify the dimensionless drag force \hat{f}_0 controlling the elasto-viscous coupling and used to design passive flow control elements for microfluidic networks.

From fur to grass fields, macroscopic surfaces covered with a dense array of anchored one-dimensional deformable structures are ubiquitous in our daily lives. When such surfaces are immersed in fluids, the feedback loop between the structure deformation and the flow can alter the flow field around them in non-trivial ways, with potential consequences for living organisms [1, 2]. Analogous hairy surfaces are also omnipresent at the microscale inside and on the surface of living organisms. Examples include the papilla of tongues [3, 4], the brush border in the gut and kidney [5], the cilia in respiratory tracts [6] or the glycocalix in blood vessels [7]. These hair-like structures perform a wide range of functions that are essential for the survival of many organisms, including humans, such as sensing or filtering for passive ones [8, 9], or transporting fluids or cells for active ones [10].

At these small scales, confinement has a strong influence on the flows that are typically laminar and exacerbates the fluid-structure interaction feedback loop. As the structure deforms, it modifies the degree of confinement and thus has a much larger impact on the fluid flow than in unconfined cases where the latter can often be neglected [11, 12]. Recently, the feedback loop between individual elastic structures and confined laminar flows has received a lot of attention since it can be harnessed for passive flow control in microchannels [13–19]. On the other hand, less is known about the fluid-structure interaction of confined dense arrays of elastic hairs akin to biological surfaces. There, collective effects enter into play and the hairy surface behavior cannot be determined from the study of single hairs [20–23].

While new numerical methods are currently being developed to tackle the fluid-structure interactions in such systems [21], only pure shear flow is so far well understood [20]; the hairy surface displays a confinement dependent non-linear drag which can be made directional by inclining the hairs. In this simple Couette flow, there is no pressure gradient and thus no flow inside the hair bed which greatly simplifies the fluid modeling [20]. However, most biological and microfluidic channels are pressure driven which will drive a significant flow inside the hair bed (see Movie S1 [24]). This inner flow needs to be characterized and accounted for in models to understand the mechanics of biological channels covered with

hair-like appendages as well as to use hairy surfaces as passive flow control devices in microfluidic chips.

Here, I investigate experimentally and theoretically pressure driven flows in channels obstructed by a dense array of elastic hairs. I show that hair flexibility generates a non-linear pressure-flow rate relationship, aka hydraulic resistance, that I rationalize with a reduced order fluid-structure interaction model. The flow inside the hairy surface is treated as a Darcy flow in an effective deformable porous media matched to a parabolic flow in the free region. This flow and its associated

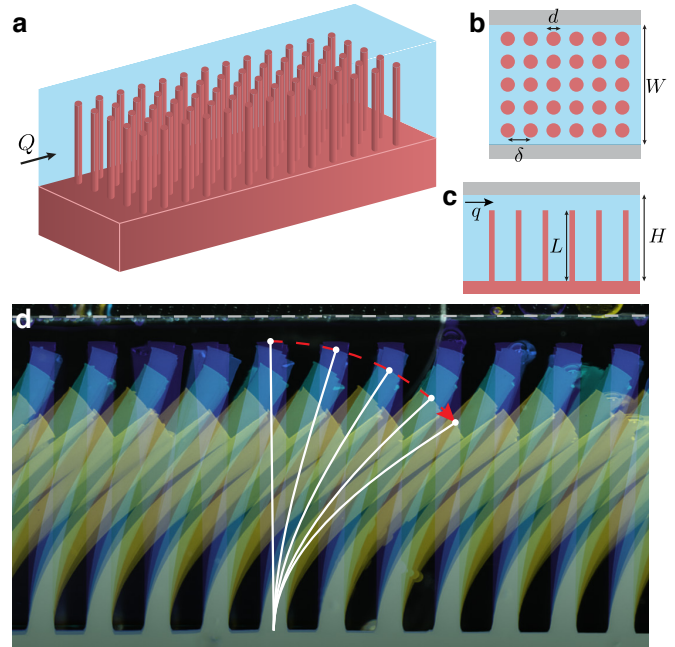


FIG. 1. (a) Schematic of the experiment, including cross-sections in the horizontal (b) and vertical (c) directions. The channel walls are omitted in (a) for clarity. (d) Superimposition of experimental images of a portion of the channel for different flow rates $Q = \{0, 2, 5, 12, 25\}$ mL/min (see also Movie S1 [24]). The centerline of a hair, its tip movement, and the channel ceiling are drawn for clarity. Parameters: $d = 0.4$ mm, $\delta = 0.83$ mm, $L = 5$ mm, $H \approx 5.5$ mm, $W = 5.4$ mm, $E = 1.27$ MPa, $\eta = 0.89$ Pa.s.

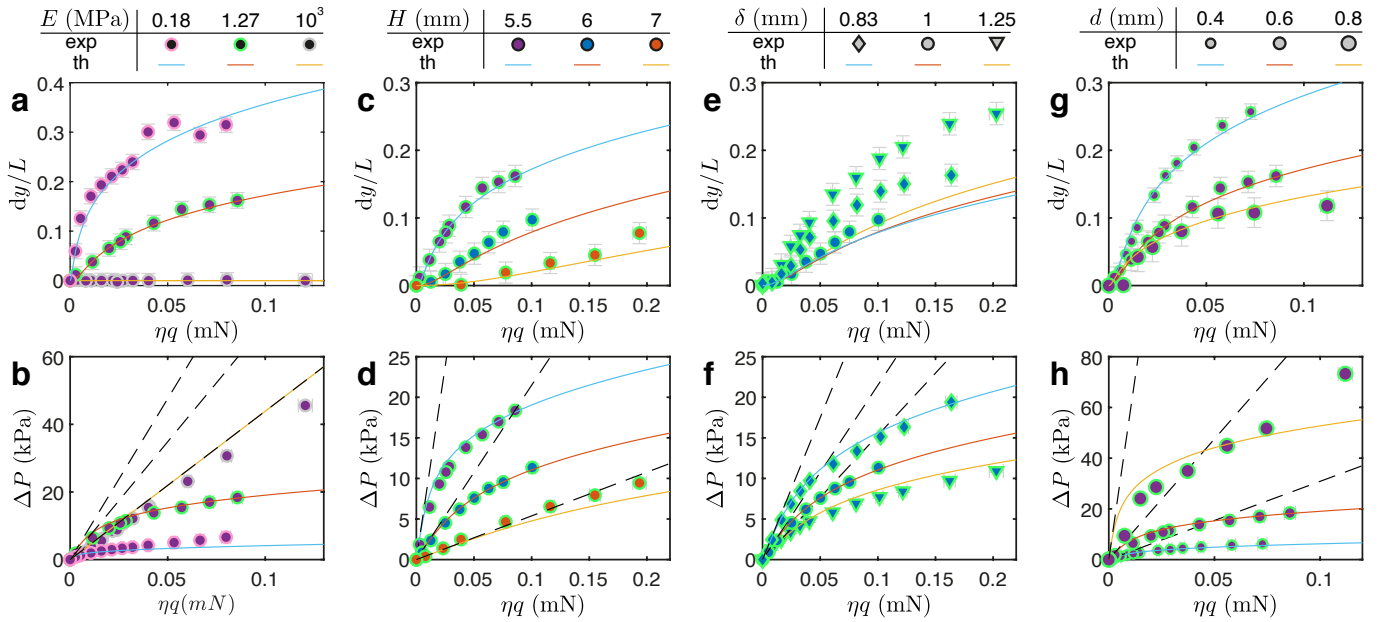


FIG. 2. Normalized vertical tip deflection dy/L and pressure difference ΔP as a function of the fluid load ηq while varying independently the bed parameters: Young modulus E (a,b), channel height H (c,d), hair spacing δ (e,f), and hair diameter d (g,h). The parameters are coded through the marker inside and outside colors, shape, and size, see legend. Error bars represent the measurement uncertainty. Colored curves are the model prediction for the same parameters, dashed black lines are the pressure-flow rate curves in the absence of deformation.

fluid loading are then coupled to a non-linear beam model for the hair deformation that dictates the porous media dimensions. This model is leveraged to identify the key dimensionless quantities governing the fluid-structure interaction problem and solved numerically to predict the hair deflection and the channel hydraulic resistance without any free parameters. These findings can then be used to design hairy surfaces for passive flow control in viscous channel networks such as relief valves, memristors, or flow rectifiers.

The experimental setup is sketched in Fig. 1a-c. Using 3d printed molds, square arrays of elastic hairs of length L , diameter d , and spacing δ are molded in silicone elastomers. These hair arrays are then inserted inside a channel carved in PMMA of width W and height H . To avoid swelling the hairs, pure glycerine is used as working fluid. The silicone elastomer Young modulus E and the glycerine viscosity $\eta(T)$, with T the room temperature recorded for each experiment, are measured in a rheometer. The fluid flow rate Q is controlled with a syringe pump and the pressure P at the inlet and outlet of the hair bed are measured with two pressure sensors. The hair deformation is recorded from the side with a camera. More details about the channel manufacturing, material characterization, and experiment procedure are shown in SM [24]. Focusing on the steady-state regime, I explore channels whose free region $H - L \ll W$ such that I expect the problem to be invariant along the channel width and define the reduced flow rate $q = Q/W$. The Reynolds number defined with the largest length scale H is small, $Re = \rho q/\eta < 0.2$ with $\rho = 1260 \text{ kg/m}^3$ the density of glycerine, and the flow is

thus laminar.

The side view of the channel during a typical experiment is shown in Fig. 1b (see also Movie S1 [24]). The hairs, initially straight and obstructing a large portion of the channel, are gradually deformed as the flow rate increases stepwise. Fig. 2 shows the normalized vertical deflection of the hair tip dy/L as well as the pressure difference ΔP across the hair bed as a function of the fluid load ηq as the hair bed parameters and channel height are varied independently. The fluid load ηq was chosen as control variable to be able to compare experiments done at different room temperatures $18.5 < T(^{\circ}\text{C}) < 26$ and thus different viscosities $0.8 < \eta(\text{Pa}\cdot\text{s}) < 1.5$.

As shown in Fig. 2a,b, a ‘rigid’ hair bed directly 3d printed with the printer resin barely deforms and exhibits a linear pressure-flow rate relationship. For ‘soft’ hairs, the vertical deflection increases with the fluid load and eventually saturates at very large flow rates. The evolution of the horizontal tip deflection dx/L is larger and qualitatively similar (see Fig. S2 [24]). The deformations being large, the hair bed’s overall height decreases significantly which opens up the free portion of the channel. As a result, the pressure-flow rate relationship is strongly sub-linear. The initial degree of confinement of the hair bed is varied in Fig. 2c,d through the channel height H . The higher the confinement, the larger the deformations for a given fluid load. A higher confinement increases the overall value of the pressure drop and decrease the fluid load at which it becomes non-linear. The hair spacing δ does not seem to have a strong influence on the hair deformation as shown in Fig. 2e,f. However, it impacts the pressure drop

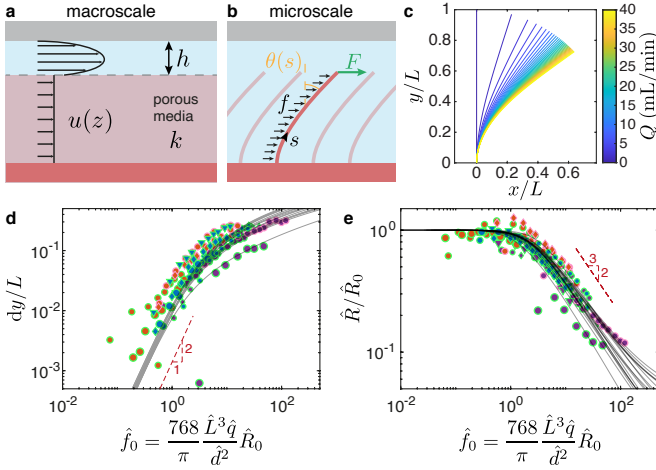


FIG. 3. **(a)** Schematic of flow modeling at the macroscale. **(b)** Schematic of hair mechanics modeling at the microscale. **(c)** Numerical solution of the fluid-structure interaction model, for the experiment in Fig. 1d. **(d,e)** Normalized vertical tip deformation dy/L (d) and normalized hydraulic resistance \hat{R}/\hat{R}_0 (e) as a function of the dimensionless drag force \hat{f}_0 for all the experiments (see Table S1 [24]). The parameters are coded through the marker inside and outside colors, shape, and size, see legend Fig. 2. The black curves are the result of the model for the same parameters.

across the channel; the tighter the array the higher the pressure drop. Increasing the hair diameter d decreases the hair deformation as they get stiffer and increases the pressure drop as it also makes the array tighter (Fig. 2g,h).

To understand the properties of these hairy channels, I first adopt a macro-scale view and model the hair array as an isotropic porous media of permeability k partially obstructing the channel as shown in Fig. 3a. Several approaches exist to model such flows and the conditions at the porous-free interface [25]. For simplicity, I use the Beavers & Joseph formulation [26] that assumes a uniform Darcy flow $u_D = -(k/\eta)\nabla P$ in the porous domain and a Poiseuille flow u_P with a slip length of size \sqrt{k}/α in the free domain of height h , with α an empirical coefficient of order 1 characterizing the porous structure:

$$u_P = -\frac{\nabla P}{2\eta} \left[(h^2 - z^2) + \frac{\alpha(h^2 - 2k)}{\sqrt{k} + \alpha h} (h - z) \right]. \quad (1)$$

Here, z is defined with respect to the porous interface. The channel hydraulic resistance (per unit width and length) $R = -\nabla P/q$ can then be computed by integrating the flow profile $q = \int_{-(H-h)}^0 u_D dz + \int_0^h u_P dz$:

$$R(h) = \frac{12\eta (\sqrt{k} + \alpha h)}{\alpha h^4 + 4\sqrt{k}h^3 + 6\alpha kh(2H - h) + 12(H - h)k^{3/2}}. \quad (2)$$

Eq. (2) can be readily used to predict the pressure drop for rigid hair beds for which $h = H - L$, provided the permeability $k = f(d, \delta)$ is known. For regular arrays of cylinders,

the permeability can be computed through asymptotic models [27, 28], scaling laws [29], or reduced numerical models [30]. For its simplicity and validity over the full range of packing fractions, I use the scaling $k = c\delta^2(1 - d/\delta)^3$ with $c = 0.1475$ [29]. Fig. 2b,d,f,h shows the pressure drop predicted by Eq. (2) with $\alpha = 1$ as dashed black lines. It captures reasonably well the pressure drop measured for ‘rigid’ hairs (see Fig. 2b) as well as the initial slope of the pressure-flowrate relationship of soft hairs. I therefore set $\alpha = 1$ in the following.

To compute the hydraulic resistance of soft hair beds, I need to predict the evolution of the gap h which results from the deformation of individual hairs at the microscale (see Fig. 3b). I need to account for large deflections and thus use non-linear beam theory. Denoting the coordinates of the hair centerline as $(x(s), y(s))$, with s the arc-length, and $\theta(s)$ the tangent angle with respect to the vertical, the force and torque balance on a hair reads:

$$\begin{aligned} EI\theta''(s) + (F(h) + f(h)(L - s)) \cos \theta(s) &= 0, \\ y'(s) = \cos \theta(s), \quad x'(s) = \sin \theta(s), & \quad (3) \\ x(0) = 0, y(0) = 0, \theta(0) = 0, \theta'(L) = 0. & \end{aligned}$$

Here, $(\cdot)' = d/ds$, $I = \pi d^4/64$, $f(h)$ is a distributed load coming from the fluid drag inside the hair bed and $F(h)$ is a concentrated load at the tip from the fluid shear stress. Both forces a priori depend on the gap h and thus the beam deflection itself since $h = H - y(L) = H - \int_0^L \cos(\theta(s)) ds$.

To compute these microscale forces, one needs to consider the details of the flow at the hair scale. Inside the hair bed, the fluid drag coming from the microscale flow is related to the permeability through momentum conservation [28]: $f = (\delta^2/k)\eta u_D = \delta^2 q R(h)$. At the hair tip, the macroscale slip boundary condition matched to u_D is not appropriate and the tangential velocity is expected to be null. Assuming a no-slip parabolic flow with the same flowrate as the macroscale one, the tip force reads $F = (\pi/8)d^2 q R(h)(\alpha h^2 + 4\sqrt{k}h + 6\alpha k)/(\alpha h + \sqrt{k})$ (see SM [24]). Combining everything yields a reduced order, fully-coupled, fluid-structure interaction model that has the form of a 1d integro-differential boundary value problem.

This model is made dimensionless using the relevant aspect ratios, $\hat{L} = L/H$, $\hat{d} = d/\delta$, $\hat{\delta} = \delta/H$, $\hat{k} = k/H^2$, and the elasto-viscous parameter $\hat{q} = \eta q/E d^2$ (see SM [24]). I solve the dimensionless equations (Eqs. (S2)(S3)(S4)) numerically with Matlab and show in Fig. 3c the hair profile as the flowrate is increased for the experimental parameters of Fig. 1d. In Fig. 2a,c,e,g, I compare the tip vertical deflection predicted by the model to the one measured experimentally and find a quantitative agreement, without any adjustable parameters. Using the computed tip deflection for h in Eq. (2) yields a prediction for the pressure drop in our channels that is compared to the experimental pressure drop in Fig. 2b,d,f,h. Here also the agreement is excellent.

To get analytical insights on the role of the various length scales in the problem, I simplify the model by neglecting the

tip force F which is small compared to the drag inside the bed f (see SM [24]). I then look for asymptotic solutions for small \hat{q} and find that up to the second order, $dx/L = \hat{f}_0/8$ and $dy/L = \hat{f}_0^2/112$ with \hat{f}_0 the dimensionless drag force for rigid hairs (see SM [24]):

$$\hat{f}_0 = \frac{768 \hat{L}^3 \hat{q}}{\pi \hat{d}^2} \hat{R}_0, \quad (4)$$

$$\hat{R}_0 = \frac{\sqrt{\hat{k} + \alpha(1 - \hat{L})}}{\alpha(1 - \hat{L})^4 + 4\sqrt{\hat{k}}(1 - \hat{L})^3 + 6\alpha\hat{k}(1 - \hat{L})^2 + 12\hat{L}\hat{k}^{\frac{3}{2}}}.$$

Here $\hat{R} = RH^3/12\eta$ is the hydraulic resistance rescaled by the one of the empty channel and \hat{R}_0 its value in the absence of deformations, i.e. for $h = H - L$.

Fig. 3d shows the tip vertical deflection for all our experiments plotted as a function of \hat{f}_0 . Surprisingly, the data not only collapse for small deformations, as expected, but also for larger deformations where the asymptotic expansion is expected to fail. Moreover, \hat{f}_0 also provides a decent collapse of the hydraulic resistance once rescaled by the rigid one as shown in Fig. 3e. The hair flexibility starts to impact the hydraulic resistance when $\hat{f}_0 \sim 1$, and I observe empirically $\hat{R}/\hat{R}_0 \sim \hat{f}_0^{-2/3}$ for large deformations. The rigid hair bed drag force \hat{f}_0 is thus an efficient control parameter encompassing both the material and geometrical properties of our system and can be used to predict the hydraulic resistance of channels obstructed by dense hair-like structures.

While efficient to describe the experiments presented here, the reduced order fluid-structure interaction model has some limitations. The two region fluid modeling is only valid for dense arrays. Besides, hair to hair contact, which can occur at large deformations, and the permeability variations due to the deformation dependent solid fraction are neglected. A discussion on these limitations is available in SM [24].

Channels obstructed by a dense array of soft hairs have several applications for passive flow control in microfluidic networks. The highly non-linear hydraulic resistance of channels obstructed by straight hairs can be used as a relief valve that triggers when $\hat{f}_0 > 1$. At normal operating pressure ($\hat{f}_0 \ll 1$), the flowrate in a dense and confined hairy channel remains low but if there is any pressure build-up above $\hat{f}_0 > 1$ the channel opens up and releases the pressure quickly. Assembling several of these fluidic ‘antifuse’ in networks could act as a memristor and encode information as recently demonstrated with soft valve networks [31]. Breaking the system symmetry by inclining the hairs (see Fig. 4a) induces a direction dependent hydraulic resistance [20, 21]. When the flow is against the grain, the hydraulic resistance increases instead of decreasing like the straight case which could be used as a fuse [32] or flow rectifier [20, 21]. For all these applications, the reduced order fluid-structure interaction model presented here, which is solved almost instantly on a laptop, can be leveraged to guide the design of the hair bed for each application.

As a proof of concept, I look at the flow rectification application with inclined hairs by simply changing the boundary

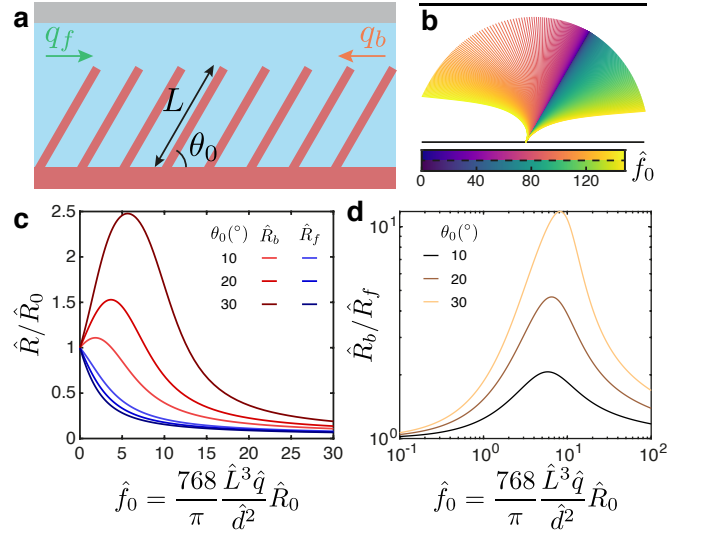


FIG. 4. (a) Schematic of a channel with hairs inclined at an angle θ_0 . The channel is now asymmetric with respect to the flow direction, forward q_f or backward q_b . (b) Model prediction for the deformation of inclined hairs with $\theta_0 = 30^\circ$. Other parameters are similar to Fig. 1d ($\hat{L} \approx 0.92$, $\hat{d} = 0.5$, $\hat{\delta} = 0.15$). The black lines indicate the channel walls and the two color maps indicate the dimensionless drag force \hat{f}_0 in the forward and backward directions. (c) Predicted normalized hydraulic resistance \hat{R}/\hat{R}_0 in the forward and backward direction as a function of \hat{f}_0 for three inclination angles ($\hat{d} = 0.5$, $\hat{\delta} = 0.15$). The initial effective porous media height, and thus R_0 , are kept constant by setting $\hat{L} = 0.8/\cos\theta_0$. (d) Ratio of the backward to forward resistance \hat{R}_b/\hat{R}_f shown in c.

condition $\theta(0) = \theta_0$ in Eq. 3. Typical numerical beam profiles for a hair bed similar to the one of Fig. 1d but inclined by $\theta_0 = 30^\circ$ are shown in Fig. 4b for forward and backward flows. In Fig. 4c I show the hydraulic resistance in the forward \hat{R}_f and backward \hat{R}_b direction as a function of the dimensionless drag force \hat{f}_0 for the same hair bed at three levels of inclination (the effective porous media height $\hat{L}\cos\theta_0$ is kept constant). The backward hydraulic resistance passes through a maximum for $\hat{f}_0 \sim 1 - 10$ signaling that there is an optimal flow rate for rectification that is evidenced in Fig. 4d which plot \hat{R}_b/\hat{R}_f as a function of \hat{f}_0 .

In summary, fluidic channels obstructed by a dense array of elastic hairs display a highly sub-linear hydraulic resistance that results from hair deformations. This non-linearity is rationalized with a macroscale two region flow model where the hair bed is treated as a compressible porous media whose height is governed by the deflection of individual hairs at the microscale. This reduced order fully coupled fluid-structure interaction model is solved numerically and shows a good agreement with experiments, without any fitting parameter. An asymptotic analysis allows to extract the key physical parameter governing the hair response \hat{f}_0 that combines an elasto-viscous parameter with the several length scales of the problem. Finally, I show how to leverage the model to design passive flow control elements in fluidic networks based on

these hairy channels.

Acknowledgments: I thank A. Rocchi for his help with the mold design and the Drahi-X Novation Center for the use of their equipment. This research was funded, in whole or in part, by l'Agence Nationale de la Recherche (ANR), project ANR-24-CE30-5885-01. For the purpose of open access, the author has applied a CC BY public copyright license to any Author Accepted Manuscript (AAM) version arising from this submission.

-
- [1] E. de Langre, Effects of wind on plants, *Annual Review of Fluid Mechanics* **40**, 141 (2008).
- [2] H. M. Nepf, Flow and transport in regions with aquatic vegetation, *Annual Review of Fluid Mechanics* **44**, 123 (2012).
- [3] C. J. Harper, S. M. Swartz, and E. L. Brainerd, Specialized bat tongue is a hemodynamic nectar mop, *Proceedings of the National Academy of Sciences* **110**, 8852 (2013).
- [4] A. Lechantre, A. Draux, H.-A. B. Hua, D. Míchez, P. Damman, and F. Brau, Essential role of papillae flexibility in nectar capture by bees, *Proceedings of the National Academy of Sciences* **118**, e2025513118 (2021).
- [5] S. Weinbaum, Y. Duan, L. M. Satlin, T. Wang, and A. M. Weinstein, Mechanotransduction in the renal tubule, *American Journal of Physiology-Renal Physiology* **299**, F1220 (2010), pMID: 20810611.
- [6] E. Loiseau, S. Gsell, A. Nommick, C. Jomard, D. Gras, P. Chanez, U. D'Ortona, L. Kodjabachian, J. Favier, and A. Viallat, Active mucos-cilia hydrodynamic coupling drives self-organization of human bronchial epithelium, *Nature Physics* **16**, 1158 (2020).
- [7] S. Weinbaum, L. M. Cancel, B. M. Fu, and J. M. Tarbell, The glycocalyx and its role in vascular physiology and vascular related diseases, *Cardiovascular Engineering and Technology* **12**, 37 (2021).
- [8] P. Satir, L. B. Pedersen, and S. T. Christensen, The primary cilium at a glance, *Journal of Cell Science* **123**, 499 (2010).
- [9] R. HU and L. PS, Particle capture mechanisms in suspension-feeding invertebrates, *Marine Ecology Progress Series* **418**, 255 (2010).
- [10] W. Gilpin, M. S. Bull, and M. Prakash, The multiscale physics of cilia and flagella, *Nature Reviews Physics* **2**, 74 (2020).
- [11] L. Guglielmini, A. Kushwaha, E. S. G. Shaqfeh, and H. A. Stone, Buckling transitions of an elastic filament in a viscous stagnation point flow, *Physics of Fluids* **24**, 123601 (2012).
- [12] Y.-N. Young, M. Downs, and C. R. Jacobs, Dynamics of the primary cilium in shear flow, *Biophysical Journal* **103**, 629 (2012).
- [13] D. C. Leslie, C. J. Easley, E. Seker, J. M. Karlinsey, M. Utz, M. R. Begley, and J. P. Landers, Frequency-specific flow control in microfluidic circuits with passive elastomeric features, *Nature Physics* **5**, 231 (2009).
- [14] M. Gomez, D. E. Moulton, and D. Vella, Passive control of viscous flow via elastic snap-through, *Phys. Rev. Lett.* **119**, 144502 (2017).
- [15] J.-F. m. c. Louf, J. Knoblauch, and K. H. Jensen, Bending and stretching of soft pores enable passive control of fluid flows, *Phys. Rev. Lett.* **125**, 098101 (2020).
- [16] M. Brandenbourger, A. Dangremont, R. Sprik, and C. Coulais, Tunable flow asymmetry and flow rectification with bio-inspired soft leaflets, *Phys. Rev. Fluids* **5**, 084102 (2020).
- [17] L. C. van Laake, J. de Vries, S. Malek Kani, and J. T. Overvelde, A fluidic relaxation oscillator for reprogrammable sequential actuation in soft robots, *Matter* **5**, 2898 (2022).
- [18] C. P. Moore, J. Husson, A. Boudaoud, G. Amselem, and C. N. Baroud, Clogging of a rectangular slit by a spherical soft particle, *Phys. Rev. Lett.* **130**, 064001 (2023).
- [19] H. Garg, P. G. Ledda, J. S. Pedersen, and M. Pezulla, Passive viscous flow selection via fluid-induced buckling, *Phys. Rev. Lett.* **133**, 084001 (2024).
- [20] J. Alvarado, J. Comtet, E. de Langre, and A. E. Hosoi, Non-linear flow response of soft hair beds, *Nature Physics* **13**, 1014 (2017).
- [21] D. B. Stein and M. J. Shelley, Coarse graining the dynamics of immersed and driven fiber assemblies, *Phys. Rev. Fluids* **4**, 073302 (2019).
- [22] C. de Blois, S. J. Haward, and A. Q. Shen, Canopy elastic turbulence: Spontaneous formation of waves in beds of slender microposts, *Phys. Rev. Fluids* **8**, 023301 (2023).
- [23] C. Ushay, E. Jambon-Puillet, and P.-T. Brun, Interfacial flows past arrays of elastic fibers, *Phys. Rev. Fluids* **8**, 044001 (2023).
- [24] See Supplemental Material at [URL will be inserted by publisher] for experimental methods, material characterization, details on the model derivation and its limits, a table summarizing the parameters of each experiment, and a supplementary movie of the experiment.
- [25] M. Le Bars and M. G. Worster, Interfacial conditions between a pure fluid and a porous medium: implications for binary alloy solidification, *Journal of Fluid Mechanics* **550**, 149–173 (2006).
- [26] G. S. Beavers and D. D. Joseph, Boundary conditions at a naturally permeable wall, *Journal of Fluid Mechanics* **30**, 197–207 (1967).
- [27] J. Happel, Viscous flow relative to arrays of cylinders, *AIChE Journal* **5**, 174 (1959).
- [28] J. Drummond and M. Tahir, Laminar viscous flow through regular arrays of parallel solid cylinders, *International Journal of Multiphase Flow* **10**, 515 (1984).
- [29] M. P. Sobera and C. R. Kleijn, Hydraulic permeability of ordered and disordered single-layer arrays of cylinders, *Phys. Rev. E* **74**, 036301 (2006).
- [30] G. A. Zampogna and A. Bottaro, Fluid flow over and through a regular bundle of rigid fibres, *Journal of Fluid Mechanics* **792**, 5–35 (2016).
- [31] A. Martínez-Calvo, M. D. Biviano, A. H. Christensen, E. Katifori, K. H. Jensen, and M. Ruiz-García, The fluidic memristor as a collective phenomenon in elasto-hydrodynamic networks, *Nature Communications* **15**, 3121 (2024).
- [32] F. Box, G. G. Peng, D. Pihler-Puzović, and A. Juel, Flow-induced choking of a compliant hele-shaw cell, *Proceedings of the National Academy of Sciences* **117**, 30228 (2020).

Supplemental Material for: Dense array of elastic hairs obstructing a fluidic channel

Etienne Jambon-Puillet

LadHyX, CNRS, Ecole Polytechnique, Institut Polytechnique de Paris, Palaiseau, France

(Dated: January 6, 2025)

In this supplementary document, I provide experimental methods, material characterization, details on the model derivation and its limits, and a table summarizing the parameters of each experiment.

I. METHODS

The hair arrays are molded with addition cure silicone elastomers (Zhermack Elite Double 8 and 32) in 3d printed molds (Asiga Max X, PlasGray v2 resin, see Fig. S1a) with the following procedure. After printing, the mold is thoroughly washed with isopropyl alcohol and then coated with a fluoropolymer (Novec 1720) to facilitate demolding. The fluoropolymer solvent is evaporated at 85°C for at least 30 min before using the mold. The silicone elastomer base and curing agent are then mixed manually at a 1:1 ratio and poured into the mold. With the more viscous elastomer (Elite Double 32), the melt can have a hard time entering the smallest holes and is thus pushed manually with a custom 3d printed piston. While the elastomer is solidifying, the excess liquid that flows through the holes under gravity is regularly wiped and additional elastomer is added to keep the mold full. After curing, the elastomer is demolded in a soapy water bath to minimize hairs sticking together. Then any hair bundle is manually separated and the hair bed is left in soapy water for a few hours to wash off any free polymer chains. All the hair arrays used here have a square arrangement, an array length $L_{\text{array}} = 51 \pm 1$ mm, a width 5 mm, and a hair length $L = 5$ mm. Three hair spacing ($\delta = \{0.83, 1, 1.25\}$ mm) and three hair diameters ($d = \{0.4, 0.6, 0.8\}$ mm) are used in the study. Smaller hairs tended to clump, while more spaced hair broke the porous media assumption.

The channels are built with milled (Datron M8Cube) and laser cut (Trotec Speedy 400) PMMA plates as shown in Fig. S1b. The central plate has been carved to insert the hair bed in a channel of height $H = \{5.5, 6, 7\}$ mm, with a removable ceiling. Tubing and screw holes have been laser cut on a side plate. Tubing holes are slightly conical to allow a snug fit with soft tubing. The channel roof and side walls are bolted with paper gasket as sealant (Klinger Statite cut with Graphtec CE6000-40) to complete the channel. The channels width, accounting for the paper sealant is $W \approx 5.4$ mm. Two pressure sensors (RS PRO 0-1 bar connected to an Arduino Uno) are connected on both sides of the hair bed.

To avoid swelling the hairs, pure glycerine (Isolatech 99.5%) is used as working fluid. Since glycerine does not wet the silicone elastomer, bubbles get entrapped inside the hairs [1] and need to be removed through manual stirring while the channel roof is open. Once the hair bed is bubble free, the roof is installed and the screws holding the three plates are tightened hard to prevent any leak that would impact the pressure measured. The fluid flow rate Q is controlled with a syringe pump (Chemyx Fusion X-4000). For each flow

rate, I let the flow run for at least 10s to allow the system to reach steady state before taking a picture with a DSLR camera (Nikon Z fc with Irix 150mm macro lens) and measuring the pressure loss. The room temperature T is recorded for each experiment. The hair tip deflection is measured manually with imageJ on a representative hair. At high flow rate, the base of the hair can slightly deform which is accounted for in the deflection measurements. The channel height H can vary slightly depending on how the roof is installed and if the base of the mold is not perfectly flat. It is thus measured for each experiment from a picture at zero flow rate. The hair length L , and hair diameter d are also measured systematically but do not deviate much from the mold values. Table. S1 recapitulates all the experiments performed and their measured parameters.

For the supplementary movie, flow tracers have been dispersed inside the glycerol (Goodfellow powder). The flow rate is increased stepwise every 30 s and the experiment is

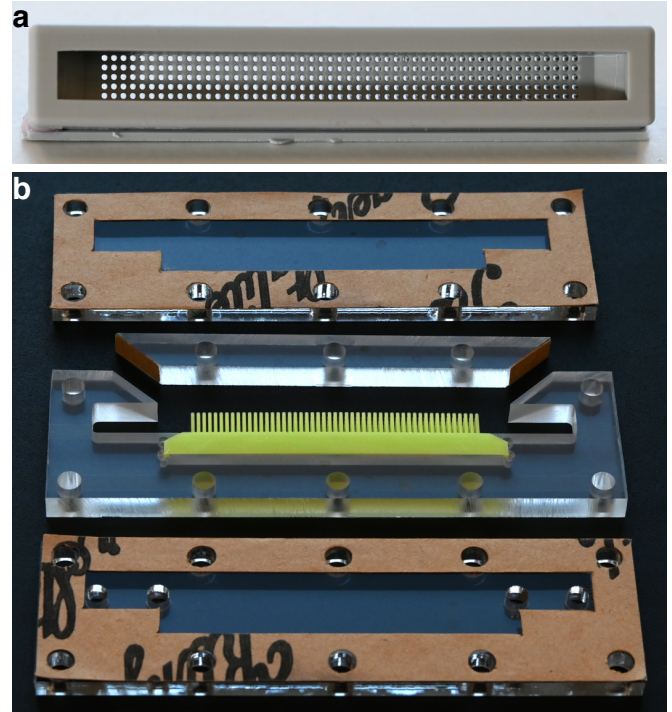


FIG. S1. (a) Picture of a mold ($d = 0.6$ mm, $\delta = 1$ mm). (b) Picture of the disassembled channel with the central plate carrying a hair bed in the middle ($H = 7$ mm).

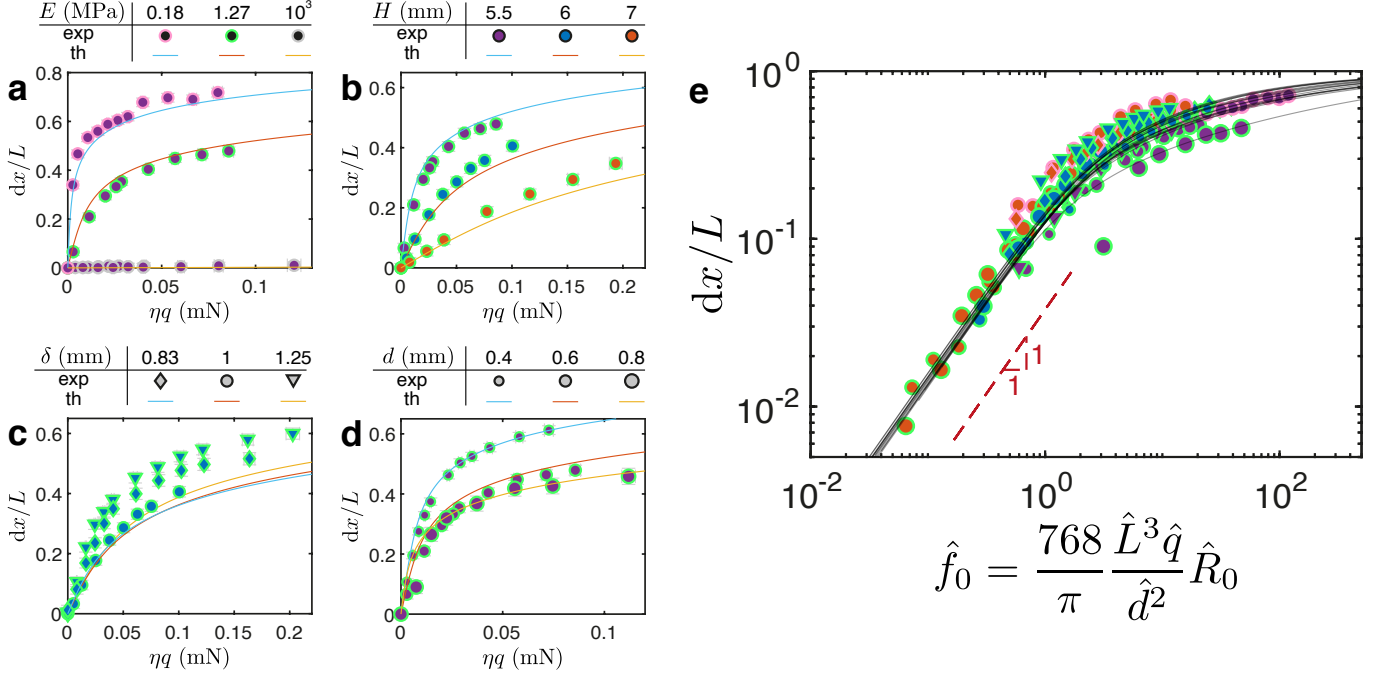


FIG. S2. **(a-d)** Normalized horizontal tip deflection dx/L as a function of the fluid load ηq while varying independently the bed parameters: Young modulus E (a), channel height H (b), hair spacing δ (c), and hair diameter d (d). The parameters are coded through the marker inside and outside colors, shape, and size, see legend. Error bars represent the measurement uncertainty. Colored curves are the model predictions for the same parameters. **(e)** Normalized horizontal tip deformation dx/L as a function of the dimensionless drag force \hat{f}_0 for all the experiments (see Table S1). Same legend as panels a-d. The black curves are the result of the model for the same parameters.

continuously shot at 120 fps. To increase the tracer visibility after compression for web use, the contrast has been increased and the image sharpened.

For brevity, only the vertical deflection dy is shown in the main text. The horizontal deflection dx was also measured and is predicted by the model. Fig. S2 shows the equivalent of Fig. 2-3 for the tip horizontal deflection.

II. MATERIAL CHARACTERIZATION

The glycerine viscosity $\eta(T)$ is measured in a rheometer (Malvern Kinexus Ultra). The viscosity is measured for shear rates $1 < \dot{\gamma} < 100$ every 0.5°C with a cone-plate geometry (2° , 60 mm) under a hood to minimize the humidity absorption. The results are shown in Fig. S3a. For a given temperature, I assume the glycerol to be Newtonian and average the viscosity value over the different shear rates. Then, I fit the mean viscosity as a function of the temperature with a quadratic function $\eta(T) = 0.005212T^2 - 0.330461T + 5.838377$ that I use to deduce the viscosity in the hairy channel experiments. After about 3 h, I remeasured the viscosity at three temperatures and found a value about 5% below the initial measurement due to the solution hydrating. I therefore neglect the effect of hydration in the channel experiments that last about 30 min in a closed environment.

The silicone elastomer Young modulus E is computed from

the oscillatory rheology of the curing melt (Malvern Kinexus Ultra). The silicone elastomer melt, mixed manually at a 1:1 ratio, is directly poured in the rheometer with a parallel plate geometry (20 mm). The storage G' and loss G'' moduli are measured under constant oscillatory shear ($\gamma = 1\%$, $f = 1$ Hz) as the melt cures as shown in Fig. S3b. The melt, initially ‘liquid’ ($G'' > G'$) becomes ‘solid’ ($G' > G''$) after ~ 15 min and eventually reach steady-state after ~ 30 min where it is fully elastic ($G' \gg G''$). The Young modulus is then $E = 2(1 + \nu)G'$ with $\nu = 0.5$ the Poisson ratio. The Young modulus of the 3d printer resin is estimated to be $E \sim 10^3$ MPa from the hardness in its technical data sheet (82 Shore D) [2].

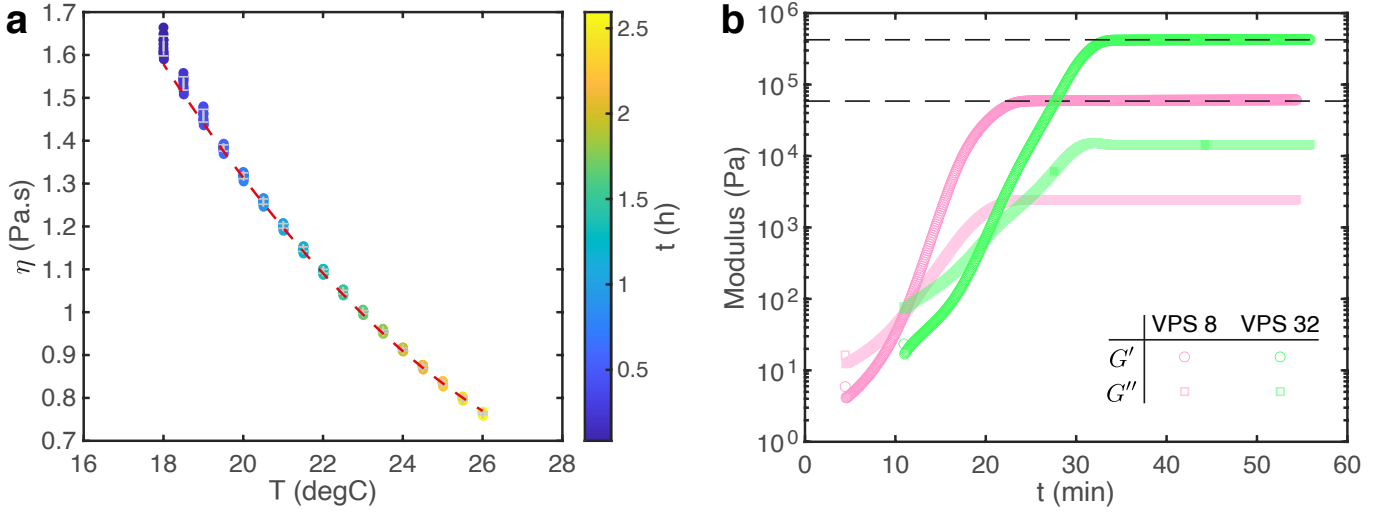


FIG. S3. **(a)** Glycerol viscosity as a function of temperature $\eta(T)$. Each colored data point is a measurement at a given shear rate $\dot{\gamma}$, color coded by the time t since the beginning of the experiment. The gray error bars are the mean and standard deviation for a given temperature. The red dashed curve is a quadratic fit. **(b)** Oscillatory rheology of the curing silicone elastomers VPS 8 (pink) and VPS 32 (green) until complete curing ($\gamma = 1\%$, $f = 1$ Hz). Opaque circles represent the storage modulus G' while semi transparent squares represent the loss modulus G'' . The dashed black lines represent the final storage modulus.

III. MODEL ADDITIONAL DETAILS

A. Tip force derivation

The tip of the hair is subject to a shear force coming from the free region $F = \frac{\pi}{4}d^2\tau_s$ with τ_s the wall shear stress on the hair tip. The velocity u_P in Eq. (1) is an average macroscale velocity and is thus not representative of the microscale flow velocity above the hair tip. In particular, the velocity is zero on the hair surface and τ_s is thus greater than $\eta \frac{du_P}{dz} \big|_0$. To estimate it, I assume that the flow field directly above the beam is still reasonably parabolic with no slip: $u^*(z) = \frac{6\bar{u}^*}{h^2}(zh - z^2)$, where \bar{u}^* is the average flow rate in this section. I then assume that this average flow rate is equal to the average flow rate in the free section of the macro model, i.e. $\bar{u}^* = \frac{1}{h} \int_0^h u_P dz$. The shear stress is then $\tau_s = \eta \frac{du^*}{dz} \big|_0$ which yields the tip force:

$$F = -\frac{\pi d^2}{8} \nabla P \frac{\alpha h^2 + 4\sqrt{k}h + 6\alpha k}{\alpha h + \sqrt{k}}. \quad (\text{S1})$$

$$\hat{R} = \frac{R}{\frac{12\eta}{H^3}} = \frac{\sqrt{\hat{k}} + \alpha(1 - \hat{L}\hat{y}(1))}{\alpha(1 - \hat{L}\hat{y}(1))^4 + 4\sqrt{\hat{k}}(1 - \hat{L}\hat{y}(1))^3 + 6\alpha\hat{k}(1 - (\hat{L}\hat{y}(1))^2) + 12\hat{L}\hat{y}(1)\hat{k}^{3/2}}, \quad (\text{S3})$$

and the forces

$$\hat{f} = \frac{768}{\pi} \frac{\hat{L}^3 \hat{q}}{\hat{d}^2} \hat{R}, \quad (\text{S4})$$

$$\hat{F} = 96\hat{L}^2 \hat{q} \frac{\alpha(1 - \hat{L}\hat{y}(1))^2 + 4\sqrt{\hat{k}}(1 - \hat{L}\hat{y}(1)) + 6\alpha\hat{k}}{\alpha(1 - \hat{L}\hat{y}(1)) + \sqrt{\hat{k}}} \hat{R}.$$

B. Nondimensionalization

The non-linear beam equation, Eq. (3), is made dimensionless by rescaling all length $\hat{s} = s/L$, $\hat{x} = x/L$, $\hat{y} = y/L$:

$$\begin{aligned} \theta''(\hat{s}) + (\hat{F} + \hat{f}(1 - \hat{s})) \cos \theta(\hat{s}) &= 0, \\ \hat{y}'(\hat{s}) &= \cos \theta(\hat{s}), \quad \hat{x}'(\hat{s}) = \sin \theta(\hat{s}), \quad (\text{S2}) \\ \hat{x}(0) = 0, \hat{y}(0) = 0, \theta(0) = 0, \theta'(1) &= 0. \end{aligned}$$

Here $\hat{F} = \frac{FL^2}{EI}$ and $\hat{f} = \frac{fL^3}{EI}$ are the dimensionless fluid forces. Now introducing the following dimensionless quantities

$$\hat{L} = \frac{L}{H}, \quad \hat{d} = \frac{d}{\delta}, \quad \hat{\delta} = \frac{\delta}{H}, \quad \hat{k} = \frac{k}{H^2} = c\hat{\delta}^2(1 - \hat{d})^{3/4},$$

I rescale the gap $\hat{h} = \frac{h}{H} = 1 - \hat{L} \int_0^1 \cos \theta d\hat{s} = 1 - \hat{L}\hat{y}(1)$, the hydraulic resistance

Here, $\hat{q} = \frac{\eta q}{Ed^2}$ is the relevant dimensionless elasto-viscous parameter for this problem. Eqs. (S2)(S3)(S4) constitute the reduced order model that I solve numerically with the Matlab solver `bvp5c`.

C. Asymptotic analysis

To get some analytical insights into the problem, I first notice that for most of the experimentally accessible parameters,

$$\frac{\hat{f}}{\hat{F}} = \frac{8 \hat{L}}{\pi \hat{d}^2} \frac{\alpha(1 - \hat{L}\hat{y}(1)) + \sqrt{\hat{k}}}{\alpha(1 - \hat{L}\hat{y}(1))^2 + 4\sqrt{\hat{k}}(1 - \hat{L}\hat{y}(1)) + 6\alpha\hat{k}} \gg 1$$

such that I consider the simplified form of Eqs. (S2)

$$\theta''(\hat{s}) + \hat{f}(1 - \hat{s}) \cos \theta(\hat{s}) = 0. \quad (\text{S5})$$

Then I look for solutions of the form $\theta(\hat{s}) = \sum_n \hat{q}^n \theta_n(\hat{s})$ with \hat{q} treated as a small parameter [3]. For straight hairs, the solution should be symmetric with respect to the flow direction and even terms are thus zero. In particular at order zero $\theta_0(\hat{s}) = 0$. At the first order in \hat{q} , $\theta(\hat{s}) = \hat{q}\theta_1(\hat{s})$ and thus $\cos \theta(\hat{s}) = \cos(\hat{q}\theta_1(\hat{s})) = 1$, and $\hat{y}(1) = \int_0^1 \cos \theta(\hat{s}) d\hat{s} = 1$. Inserting this in eq. (S5) yield at first order

$$\begin{aligned} \hat{q}\theta_1''(\hat{s}) + \hat{f}_0(1 - \hat{s}) &= 0, \\ \hat{f}_0 &= \frac{768 \hat{L}^3 \hat{q}}{\pi \hat{d}^2} \hat{R}_0, \\ \hat{R}_0 &= \frac{\sqrt{\hat{k}} + \alpha(1 - \hat{L})}{\alpha(1 - \hat{L})^4 + 4\sqrt{\hat{k}}(1 - \hat{L})^3 + 6\alpha\hat{k}(1 - \hat{L})^2 + 12\hat{L}\hat{k}^{\frac{3}{2}}}. \end{aligned} \quad (\text{S6})$$

Note that eq. (S6) is mathematically equivalent to a linear beam model under a uniform distributed load whose solution is

$$\theta_1(\hat{s}) = \frac{\hat{f}_0}{6\hat{q}} (\hat{s}^3 - 3\hat{s}^2 + \hat{s}). \quad (\text{S7})$$

Since $\theta_2(\hat{s}) = 0$ by symmetry, eq. (S7) is valid up to the second order in \hat{q} .

This analysis suggests that the four dimensionless parameters \hat{q} , \hat{L} , $\hat{\delta}$, and \hat{d} can be combined in a single one: \hat{f}_0 . This small \hat{q} / small slope solution can then be used to compute the

tip deflection

$$\begin{aligned} \hat{x}(1) &= \int_0^1 \sin \theta d\hat{s} \approx \int_0^1 \hat{q}\theta_1 d\hat{s} \approx \frac{\hat{f}_0}{8}, \\ \hat{y}(1) &= \int_0^1 \cos \theta d\hat{s} \approx \int_0^1 \left(1 - \frac{(\hat{q}\theta_1)^2}{2}\right) d\hat{s} \approx 1 - \frac{\hat{f}_0^2}{112}. \end{aligned} \quad (\text{S8})$$

D. Model limitations

The Beavers & Joseph formulation of the flow field inside and outside the hair bed assumes that we can separate a porous region from a free region. This is reasonable when the size of the free region is much larger than the typical pore size, i.e. $h \gg \sqrt{k}$ [4]. A criterion for the effective porous media model to be valid would thus be $H - L \gg \sqrt{k}$ and a different type of flow modeling is needed for sparse hair beds.

The beam model does not account for hair-to-hair contact which would effectively ‘rigidify’ the hairs and impact the hydraulic resistance. Given the hairs’ finite size, contact is eventually bound to happen as the flow rate increases since at infinite flow rate the hairs completely lie down on the surface. The critical contact flow rate can be extracted from the model by checking whether two computed beam profiles of thickness d separated by δ intersect. While performing this analysis is outside of the scope of this paper, contact is expected to be a concern for tighter hair beds for which $\delta - d$ is small and/or very soft hairs. In practice, contact was observed at high flowrate for very packed or very soft hair beds (Experiments 13,16,21,24,27 in Table. S1) with in most cases only small deviations from the contactless model (the exception being the experiments shown in Fig. 2h with $d = 0.8$ mm and $\delta = 1$ mm).

Finally, as the hairs bend, the solid packing fraction increases at the top of the bed and impacts the permeability which is no longer uniform. In the horizontal cross section (see Fig. 1b), the projection of the bent beam will turn into ellipses elongated in the flow direction with semi axes $a = \frac{d}{2 \cos \theta(s)}$ and $b = d/2$. While this effect can be computed from the model which solves for $\theta(s)$, and in principle integrated as a deflection dependent permeability $k(\theta(s)) = f(d, \delta, \theta(s))$, doing so is out of the scope of this letter. Here also, the effect is expected to be larger at high packing fraction since k is more sensitive to changes in solid fraction than [5].

-
- [1] C. Ushay, E. Jambon-Puillet, and P.-T. Brun, Interfacial flows past arrays of elastic fibers, *Phys. Rev. Fluids* **8**, 044001 (2023).
 - [2] H. J. Qi, K. Joyce, and M. C. Boyce, Durometer hardness and the stress-strain behavior of elastomeric materials, *Rubber Chemistry and Technology* **76**, 419 (2003).
 - [3] J. Alvarado, J. Comtet, E. de Langre, and A. E. Hosoi, Nonlinear

- flow response of soft hair beds, *Nature Physics* **13**, 1014 (2017).
- [4] G. S. Beavers and D. D. Joseph, Boundary conditions at a naturally permeable wall, *Journal of Fluid Mechanics* **30**, 197–207 (1967).
- [5] M. P. Sobera and C. R. Kleijn, Hydraulic permeability of ordered and disordered single-layer arrays of cylinders, *Phys. Rev. E* **74**, 036301 (2006).

Experiment number	Material	H (mm)	L (mm)	d (mm)	δ (mm)	T ($^{\circ}\text{C}$)	Q_{max} (mL/min)
8	PlasGray v2	5.76	4.96	0.57	1	24.4	15
10	VPS 32	5.42	4.92	0.42	1	23.6	25
11	VPS 32	5.43	4.98	0.43	0.83	24.3	25
12	VPS 32	5.42	4.95	0.62	1	23.8	25
13	VPS 8	5.39	4.92	0.59	1	24.6	30
14	VPS 32	7.09	4.91	0.64	1	25.0	40
15	VPS 32	6.15	4.91	0.62	1	25.3	40
16	VPS 8	7.09	4.83	0.62	1	21	40
17	VPS 32	7.01	4.89	0.61	1	20.5	40
19	VPS 32	6.07	4.91	0.43	0.83	20.9	40
21	VPS 8	6.96	4.92	0.62	1	21.1	40
22	PlasGray v2	5.73	4.92	0.58	1	20.1	30
23	VPS 32	5.51	4.89	0.81	1.25	21.4	40
24	VPS 32	5.21	4.83	0.83	1	20.9	30
25	VPS 32	6.52	4.83	0.84	1	20.8	40
26	VPS 32	5.88	4.87	0.83	1	21.1	40
27	VPS 8	6.99	4.85	0.61	0.83	20.9	40
28	VPS 32	6.02	4.88	0.62	0.83	19.9	40
29	VPS 32	6.08	4.92	0.63	1.25	20.0	50
30	VPS 32	6.13	4.86	0.40	1	18.7	30

TABLE S1. Parameters for all the experiments shown in the main text.